EDGE ARTICLE

Room-temperature ferroelectric and ferroelastic orders coexisting in a new tetrafluoroborate-based perovskite†

Xiao-Xian Chen,[a] Xiao-Yue Zhang, [b] De-Xuan Liu,[a] Rui-Kang Huang,[a] Sha-Sha Wang,[a] Li-Qun Xiong,[b] Wei-Xiong Zhang [*a] and Xiao-Ming Chen[a]

The coexistence of multiferroic orders has attracted increasing attention for its potential applications in multiple-state memory, switches, and computing, but it is still challenging to design single-phase crystalline materials hosting multiferroic orders at above room temperature. By utilizing versatile ABX_3-type perovskites as a structural model, we judiciously introduced a polar organic cation with easily changeable conformations into a tetrafluoroborate-based perovskite system, and successfully obtained an unprecedented molecular perovskite, (homopiperazine-1,4-diium)[K(BF$_4$)$_3$], hosting both ferroelectricity and ferroelasticity at above room temperature. By using the combined techniques of variable-temperature single-crystal X-ray structural analyses, differential scanning calorimetry, and dielectric, second harmonic generation, and piezoresponse force microscopy measurements, we demonstrated the domain structures for ferroelectric and ferroelastic orders, and furthermore disclosed how the delicate interplay between stepwise changed dynamics of organic cations and cooperative deformation of the inorganic framework induces ferroelectric and ferroelastic phase transitions at 311 K and 455 K, respectively. This instance, together with the underlying mechanism of ferroic transitions, provides important clues for designing advanced multiferroic materials based on organic–inorganic hybrid crystals.

Introduction

Multiferroics, in which two or more ferroic orders (including electric, elastic, and magnetic ones) coexist, have attracted much attention due to their potential applications in multiple-state memory, switches, and computing. Parallel to intensive studies on inorganic multiferroics,[1–3] the exploration of multiferroic materials has been extended to organic–inorganic hybrid materials, as they may serve as a supplement to inorganic ones in next generation flexible devices, benefiting from their mechanical flexibility, mild synthesis, and easy processing to thin films.[4–10] In particular, ABX_3-type molecular perovskites, in which each site can hold diverse components, are regarded as an important host–guest structural model for searching for molecule-based multiferroic materials.[11–17] For example, some metal formate perovskites, (Me$_2$NH$_2$)[M(HCOO)$_3$] (M = Mn^{II},

Fe^{II}, Co^{II}, Ni^{II}),[18] reveal magnetic and electric orders at below 36 K. Two ferroelastic perovskites, (Et$_3$P(CH$_2$)$_2$F/Et$_3$P(CH$_2$)$_2$Cl)–[Mn(N(CN)$_2$)$_3$],[19] display antiferromagnetic orders at below 2.4 K. An azido perovskite, (Me$_4$N)[Mn(N$_3$)$_3$],[20,21] was suggested as a multiferroic material with the coexistence of anti-ferroelectricity, ferroelasticity, and magnetic bistabilities at room temperature. Nevertheless, multiferroic materials with the coexistence of ferroelectric and ferroelastic orders, especially those occurring at above room temperature, are very scarce. Very recently, Wang *et al.* demonstrated interesting coupled ferroelasticity and ferroelectricity in a hexagonal perovskite system,[22] in which a ferroelastic switch with a large shear strain of up to 21.5% could be driven by an electric field and yield a recorded piezoelectric coefficient d_{35} of up to 4800 pm V^{-1}.

In the past decade, much effort was devoted to constructing molecular perovskites for wide usage, by utilizing multi-atomic X-bridging ligands, such as cyano, azido, thiocyanate, nitrate, and dicyanamide.[23–29] For instance, by employing the tetrahedral perchlorate ion (ClO$_4^-$), we recently constructed a large family of molecular perovskites for use as promising practical high-energy materials.[30–32] Similarly, as another well-known tetrahedral ion, tetrafluoroborate (BF$_4^-$) attracts increasing attention with an expectation to serve as a bridging ligand for constructing molecular perovskites. Since the first

[a]MOE Key Laboratory of Bioinorganic and Synthetic Chemistry, School of Chemistry, Sun Yat-Sen University, Guangzhou 510275, China. E-mail: zhangwx6@mail.sysu.edu.cn

[b]State Key Laboratory of Optoelectronic Materials and Technologies, School of Physics, Sun Yat-Sen University, Guangzhou 510275, China

† Electronic supplementary information (ESI) available: Additional data and a video of ferroelastic domain evolution. CCDC 1988358, 1988359, 1988360 and 1988361. For ESI and crystallographic data in CIF or other electronic format see DOI: 10.1039/d1sc01345a

tetrafluoroborate-based perovskite, $(H_2dabco)(NH_4)(BF_4)_3$ (H_2dabco^{2+} = 1,4-diazabicyclo[2.2.2]octane-1,4-diium), was reported by Liu *et al.* in 2011,[33] efforts to date have led to five instances.[34–37] In detail, replacing the NH_4^+ cation with alkali ions yielded three analogues, $(H_2dabco)[M'(BF_4)_3]$ (M' = Na^+, K^+, Rb^+), which undergo reversible phase transitions at 403, 410, and 333 K, respectively, accompanied by step-like dielectric switches[34,36,37] and considerable latent heats for potential heat storage. Recently, changing the A-site cations yielded two analogues, $(H_2pz)[Na(BF_4)_3]$ (H_2pz^{2+} = piperazine-1,4-diium)[34] and $(H_2mdabco)(NH_4)(BF_4)_3$ ($H_2mdabco^{2+}$ = 1-methyl-1,4-diazabicyclo-[2.2.2]octane-1,4-diium),[35] which were found to undergo phase transitions at 405 K and 368 K, respectively. However, only $(H_2pz)[Na(BF_4)_3]$ was reported to crystallize in a polar space group ($P4_3$) at room temperature but its high-temperature phase is unknown; all the other known phases in these six instances are centrosymmetric structures, and no ferroelectric or ferroelastic phase has been identified in these tetrafluoroborate-based perovskites.

Aiming to establish ferroic order for tetrafluoroborate-based perovskites, we judiciously chose a polar cation, homopiperazine-1,4-diium (H_2hpz^{2+}), to assemble with alkali ions and the tetrafluoroborate ion. Compared with the H_2pz^{2+} cation, the H_2hpz^{2+} cation with an additional –CH_2– group possesses a relatively larger dipole moment of *ca.* 2.1 D (Scheme 1), and moreover, has a more flexible configuration to break the mirror symmetry thus facilitating the establishment of a reversible polarization.

Our efforts successfully yielded an unprecedented tetrafluoroborate-based multiferroic crystal, $(H_2hpz)[K(BF_4)_3]$ (**1**), revealing both ferroelectric and ferroelastic orders at above room temperature. Herein, we disclose how the delicate interplay between the stepwise changed molecular dynamics of the organic cation and the synergistic deformation of inorganic framework essentially induces three-step phase transitions and the ferroic orders in **1**, by using the combined techniques of variable-temperature single-crystal X-ray structural analyses, differential scanning calorimetry (DSC), and dielectric, second harmonic generation (SHG) effect, and piezoresponse force microscopy (PFM) measurements.

Experimental section

Materials and instrumentations

All chemicals were commercially available and used without further purification. Powder X-ray diffraction (PXRD) patterns were recorded using a Bruker D8 ADVANCE X-ray powder diffractometer (Cu Kα, λ = 1.54184 Å). Thermogravimetric

Scheme 1 H_2pz^{2+} and H_2hpz^{2+} cations in a chair configuration.

analysis was performed using a STA 449 F3 Jupiter system with a heating rate of 10 K min^{-1} under a nitrogen atmosphere. DSC measurements were performed by heating/cooling the powder sample at a rate of 10 K min^{-1} on a TA DSC Q2000 instrument.

Dielectric permittivity was measured using an Agilent Impedance Analyser in a Mercury iTC cryogenic environment controller of an Oxford Instrument for a powder pellet sample at a rate of 3 K min^{-1}. The SHG effect was measured using a XPL1064-200 instrument at a heating/cooling rate of 3 K min^{-1}. The observation of ferroelastic domains was performed on an OLYMPUS BX41 polarizing microscope. The ferroelectric hysteresis loop was measured on a Radiant Precision Premier II. PFM measurements were performed by using a PFM mode on an Asylum MFP-3D Infinity atomic force microscope. Conductive Cr/Pt-coated silicon probes (Multi75E-G, Budget Sensors) were used in the PFM tests.

Synthesis

Stoichiometric quantities of homopiperazine (301 mg, 3 mmol) and KBF_4 (378 mg, 3 mmol) were dissolved into 2 mL and 3 mL water, respectively. After mixing these two solutions, excessive fluoroboric acid (50 wt%, 1.5 mL) was added to the mixed solution. The filtered solution was placed in a desiccator and allowed to evaporate slowly at room temperature. After about 7 days, colourless block crystals of **1** were obtained from solution in a yield of 42% based on KBF_4. The purity of the bulk phase was verified by PXRD (Fig. S1†).

Single-crystal X-ray diffraction analyses

Diffraction data at 293 K were collected on a Rigaku XtaLAB P300DS single-crystal diffractometer by using graphite monochromated Cu Kα (λ = 1.54184 Å) radiation. Absorption corrections were applied by using the multi-scan program CrysAlisPro. Diffraction data at 338 K and 400 K were collected at BL17B of the National Centre for Protein Sciences Shanghai and Shanghai Synchrotron Radiation Facility (λ = 0.77488 Å). Data reduction and absorption corrections were applied by using the APEX3 and HKL3000 program, respectively. Diffraction data at 463 K were collected on a SuperNova single-crystal diffractometer by using Mo Kα (λ = 0.71073 Å) radiation. Absorption corrections were applied by using the multi-scan program CrysAlisPro. All structures were solved by the direct methods and refined by the full-matrix least-squares technique with the SHELX program package on Olex^2.[38,39] Anisotropic thermal parameters were applied to all non-hydrogen atoms. The hydrogen atoms were generated geometrically. Crystal data as well as details of data collection and refinements for **1** are summarized in Table 1. CCDC numbers 1988358, 1988359, 1988360, and 1988361 contain the ESI crystallographic data for **1**.†

Results and discussion

Thermal analyses

Thermogravimetric analysis showed that **1** is stable up to 495 K under a nitrogen atmosphere (Fig. S2†). Three structural phase
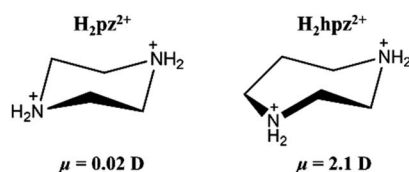
Table 1 Crystallographic data and structural refinement parameters for **1**

Complex	$(H_2hpz)[K(BF_4)_3]$ (**1**)			
Formula	$C_5H_{14}N_2B_3F_{12}K$			
Formula weight	401.71			
Temperature/K	463(2)	400(2)	338(2)	293(2)
Phase	α	β	γ	δ
Crystal system	Cubic	Orthorhombic	Orthorhombic	Orthorhombic
Space group	$Pm\bar{3}m$	$Cmcm$	$Pbcm$	$Pbc2_1$
a/Å	7.296(2)	10.568(2)	10.5005(4)	10.2792(1)
b/Å	7.296(2)	9.929(2)	9.7685(4)	9.3759(1)
c/Å	7.296(2)	14.249(3)	14.0216(5)	14.5388(2)
V/Å^{-3}	388.4(2)	1495.2(5)	1438.2(1)	1401.20(3)
Z	1	4	4	4
D_c/(g cm^{-3})	1.717	1.784	1.855	1.904
R_1 $[I > 2\sigma(I)]^a$	0.0793	0.0772	0.0678	0.0344
wR_2 $[I > 2\sigma(I)]^b$	0.1678	0.2331	0.2200	0.0962
R_1 (all data)	0.1483	0.0790	0.0769	0.0356
wR_2 (all data)	0.2237	0.2423	0.2297	0.1019
GOF	0.928	1.039	1.088	1.085
Flack parameter	—	—	—	0.06(2)
CCDC number	1988361	1988360	1988359	1988358

^{a} $R_1 = \sum ||F_o| - |F_c||/\sum |F_o|$. ^{b} $wR_2 = [\sum w(F_o^2 - F_c^2)^2/\sum w(F_o^2)^2]^{1/2}$.

transitions were detected by DSC (Fig. 1), as clearly indicated by three reversible thermal anomalies at 455/457 K (T_1), 384/383 K (T_2), and 311/315 K (T_3) during the cooling/heating runs, respectively. The total entropy changes (ΔS) of the three phase transitions in the cooling process are estimated to be 5.0, 11.6, and 24.1 J mol^{-1} K^{-1}, respectively. For convenience, we use α, β, γ, and δ to label the phases above T_1, between T_1 and T_2, between T_2 and T_3, and below T_3, respectively.

Crystal structures for the four phases

To understand the step-by-step structural phase transitions, variable-temperature single-crystal X-ray diffractions were performed for the four phases of **1**. As shown in Fig. 2, the crystal structure of **1** can be topologically assigned as an ABX$_3$-type perovskite structure. Each K$^+$ ion acting as a B-site component is coordinated by twelve F atoms from six adjacent tetrafluoroborates, all of which act as X-site bridging ligands

linking two adjacent K$^+$ ions, thus leading to a three-dimensional cage-like inorganic host framework constructed by corner-sharing K(BF$_4$)$_6$ octahedra. Each organic cation residing in each cage acts as an A-site component in the perovskite structure.

By and large, the three-step phase transitions at decreasing temperatures are highly associated with the gradually frozen molecular dynamics of H$_2$hpz^{2+} cations and cooperative deformation of the [K(BF$_4$)$_3$]$^{2-}$ inorganic framework. In detail, the α phase crystallizes in the cubic space group $Pm\bar{3}m$ (no. 221) which is the prototype of an ideal perovskite structure without any deformation. As required by the imposed crystallographic symmetry, the organic cations are 48-fold dynamically disordered in almost arbitrary orientations, and the BF$_4^-$ bridges are 16-fold disordered. In the β phase, an obvious deformation of the framework occurs, including column shifts of connected KX$_6$ octahedra, tilting distortions between adjacent octahedra, and displacements inside the octahedra,[40–43] among which the column shifts with an extended Glazer's notation of $a^Xa^Xc^0$, via coupling with the latter two parts, resulting in the space group $Cmcm$ (no. 63) for the β phase. Consequently, the organic cations become 4-fold disordered about two mirror planes perpendicular to the a- and c-axes, respectively, and all the BF$_4^-$ bridges are disordered over four sites.

With further cooling to the γ phase, the organic cations are frozen to be 2-fold disordered and two thirds of the BF$_4^-$ bridges are frozen in an ordered state. Meanwhile K$^+$ ions are slightly displaced in the ab plane, eventually resulting in a deformation of the framework with unconventional tilts (Fig. S10†) and the lower-symmetric space group $Pbcm$ (no. 57) for the γ phase. Moreover, when cooling **1** into the δ phase, a multiple tilting distortion with Glazer's notation $a^-a^-c^-$, together with an intra-octahedron displacement of K$^+$ ion towards one of the eight faces of K(BF$_4$)$_6$ octahedron, intensifies
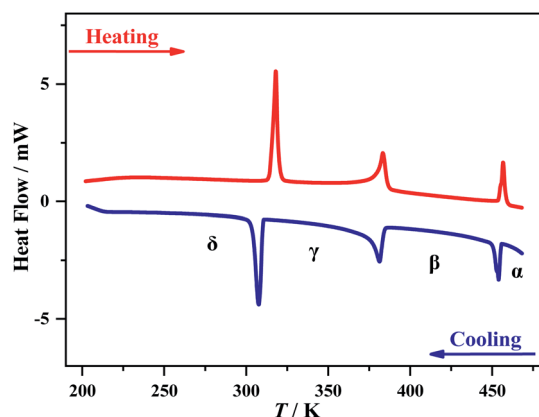

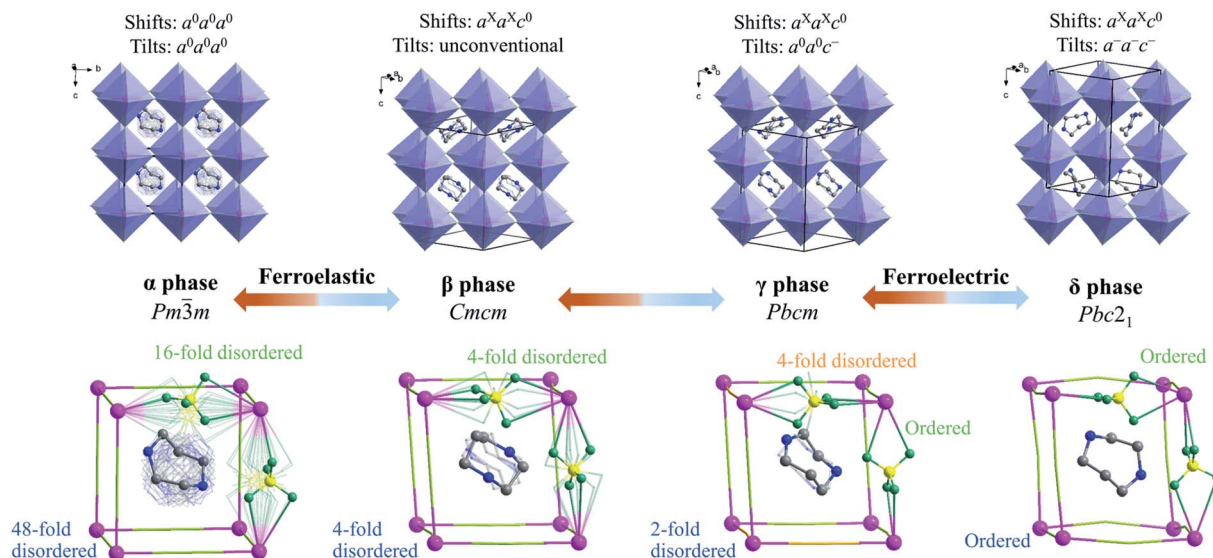**Fig. 1** DSC curves for **1** during a cooling–heating cycle.

Fig. 2   Crystal structures of **1** at four phases. The blue and aqua (or orange) notes mark the different states for H_2hpz^{2+} organic cations and BF_4^- bridging ligands, respectively. The K, C, N, B, and F atoms are shaded in purple, gray, blue, yellow, and dark green, respectively. For clarity, H atoms are omitted, and only crystallographically independent BF_4^- anions are shown while the rest are simplified into aqua or orange bars.

the deformation of the inorganic framework. More importantly, such a deformed framework hosts the polar organic cations in an orientationally ordered manner, which gives rise to a spontaneous electric polarization in the δ phase belonging to the polar space group $Pbc2_1$ (no. 29). It is noted that the tilts and displacements that occur in the δ phase are the same as those observed in inorganic perovskite ferroelectric $NaNbO_3$,[44] implying that the deformation of the inorganic framework in **1** makes an important contribution to the spontaneous polarization as well.

In short, with decreasing temperature from 463 K to room temperature, the space group of **1** transforms from $Pm\bar{3}m$ (no. 221) into $Cmcm$ (no. 63), then $Pbcm$ (no. 57), and finally to $Pbc2_1$ (no. 29), including a ferroelastic and a ferroelectric phase transition with Aizu notation of $m3mFmmm$ and $mmmFmm2$,[45] respectively (*vide infra*). Such dynamic transition of molecular components from a "melt-like" state at high temperature to a frozen state at low temperature was similarly observed in other molecular perovskites,[46,47] but **1** is a unique one that displays multi-step phase transitions to host both ferroelectric and ferroelastic orders (*vide infra*), benefiting from the delicate interplay between the frozen organic cations and the synchronously deformed inorganic framework.

Ferroelastic phase transition and spontaneous strain

During the α → β transition, a symmetry break occurs with the total symmetry decreasing from forty-eight symmetric elements (E, $8C_3$, $6C_4$, $6C_2$, $3C_2'$, i, $6S_4$, $8S_6$, $3\sigma_h$, and $6\sigma_d$) in point group O_h to eight elements (E, C_2, $2C_2'$, i, σ_h, and $2\sigma_v$) in point group D_{2h}, which is a ferroelastic transition with an Aizu notation of $m3mFmmm(ss)$ or $m3mFmmm(pp)$. From the cubic paraelastic phase (α) to the orthorhombic ferroelastic phase (β), the c-axis length is doubled, and the diagonals $b - a$ and $a + b$ in the cubic

phase become the a- and b-axes in the orthorhombic phase, respectively (Fig. 3e). Such a relationship between the unit cells of paraelastic and ferroelastic phases was similarly observed in inorganic crystals KCN and NaCN,[49] and they should be classified as a $m3mFmmm(ss)$ ferroelastic species, in which two of three mirror planes of the ferroelastic phase (β) are along the
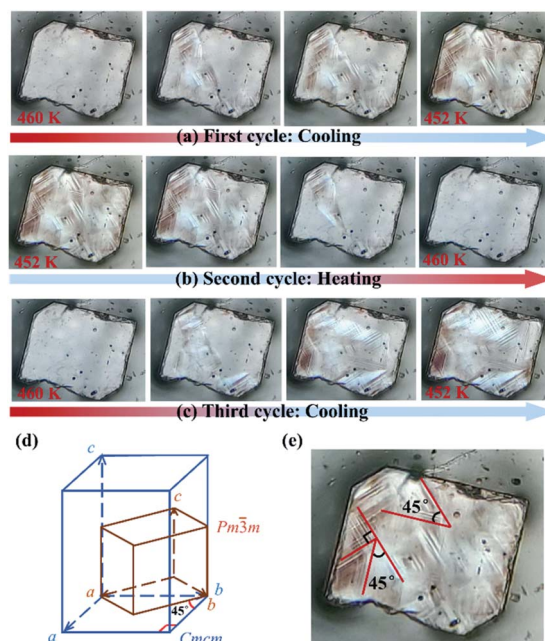

Fig. 3   Evolution of multi-domain structures between the ferroelastic phase (at 452 K) and paraelastic phase (at 460 K) in the first cooling run (a), the first heating run (b), and the second cooling run (c). (d) Schematic diagram of the transformation of unit cells between α and β phases. (e) The enlarged view of the domain structure at 452 K.

mirror planes making an angle of 45° to the tetrad axes of the paraelastic phase (α).[45]

To further verify the ferroelastic phase transition, the variation of domains between α and β phases was inspected using a polarizing microscope on a single crystal of **1** along its *c*-axis (Fig. S9†). As shown in Fig. 3a, the single crystal without any external strain reveals a mono-domain morphology at 460 K (*i.e.*, in paraelastic phase). During the α → β transition, *via* cooling the crystal to 452 K, four kinds of recognizable striated domains mixed up with some dim areas appeared and extended gradually to the entire crystal. The domain walls intersecting at angles of 45° and 90° (Fig. 3e) well match with the aforementioned transformation of unit cells during this ferroelastic transition (Fig. 3d). When the crystal was heated back to 460 K, these striated domains fade out and the mono-domain state was recovered (Fig. 3b). Such a process is repeatable, as confirmed by the appearance of multi-domain structures when the crystal was cooled again to the β phase (Fig. 3c). It should be noted that, for a *m3mFmmm*(*ss*) ferroelastic species, the number of orientation states in the ferroelastic phase is equal to the order of the point group O_h divided by the order of the point group D_{2h}, which is six for the β phase, including the four orientation states in the present domains observed along the *c*-axis.[48]

In addition, for the present *m3mFmmm*(*ss*) species, based on the aforementioned lattice parameters measured at 463 K and 400 K, a total spontaneous strain is estimated by:

$$\varepsilon_s = \sqrt{\left(2a^2 + 2b^2 + c^2 - 2ab - \sqrt{2}\,ac - \sqrt{2}\,bc\right) \Big/ 6a_0^2} = 0.0459$$

where *a*, *b*, and *c* are the lattice parameters in the orthorhombic ferroelastic phase and a_0 is that in the cubic paraelastic phase. The calculated value of spontaneous strain for **1** is 0.0459 (for details, see the ESI†), about ten times higher than that in an inorganic perovskite ferroelastic NaMgF$_3$ (ε_s = 0.004)[49] with a similar *m3mFmmm*(*ss*) phase transition.

Ferroelectric phase transition and spontaneous polarization

The γ → δ transition belongs to a ferroelectric transition with an Aizu notation of *mmmFmm*2, during which the number of total symmetric elements decreases from eight (E, C_2, $2C_2'$, i, σ_h, and $2\sigma_v$) in point group D_{2h} to four (E, C_2, and $2\sigma_v$) in point group C_{2v}. Such a change in the number of symmetric elements implies that **1** is a uniaxial ferroelectric in its room-temperature phase. To further confirm the ferroelectric ordering for the δ phase, dielectric, SHG, and PFM measurements were performed.

The temperature-dependent dielectric permittivity ($\varepsilon = \varepsilon' + i\varepsilon''$) was evaluated in the range of 285–335 K on the powder-pressed sample of **1**. As shown in Fig. 4a, the real part of the dielectric permittivity exhibits a fast step-like response around T_3 (from γ to δ phase), varying from a relatively higher dielectric state (*ca.* 3.6 for γ phase) to a relatively lower dielectric state (*ca.* 2.9 for δ phase) upon cooling. The tendency is inverted in a heating process, and a thermal hysteresis of 11.8 K was observed, in agreement with the reversible phase transition observed by DSC measurements. Such a step-like dielectric
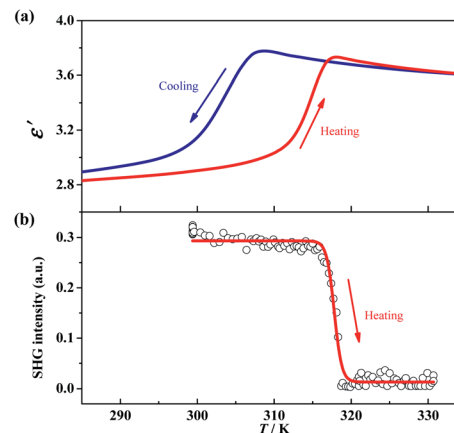

Fig. 4 The real part of dielectric permittivity during a cooling–heating cycle measured under an ac electric field with a frequency of 74 kHz (a) and temperature-dependence of the SHG signal in a heating run from 300 K to 330 K (b) for **1**.

anomaly during a ferroelectric phase transition is a unique characteristic of an improper ferroelectric.

Variable-temperature SHG measurements were performed on the polycrystalline sample of **1**. As shown in Fig. 4b, at the δ phase (below 310 K), the SHG intensity is nonzero (about 0.3 times of KH$_2$PO$_4$), *i.e.*, SHG being activated. When heating the sample to above 320 K (γ phase), the SHG intensity decreases to almost zero, *i.e.*, SHG being silenced. Such SHG switch suggests a structural phase transition from a non-centrosymmetric one to a centrosymmetric one, and well matches with the change of the space group between the δ (*Pbc*2$_1$) and γ (*Pbcm*) phases observed in single-crystal X-ray diffraction.

Ferroelectric polarization reversal was further evidenced by the *P–E* hysteresis loops (Fig. 5), which were obtained by measurements performed on a single crystal with 0.18 mm thickness using a modified Saywer–Tower circuit under a varying electric field up to 49 kV cm^{-1}, giving an estimated spontaneous polarization of 4.8 μC cm^{-2} by the extrapolation method. It should be noted that, the spontaneous electric
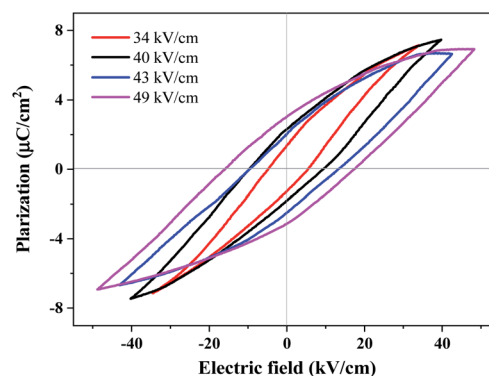

Fig. 5 Room-temperature *P–E* hysteresis loops measured on a single crystal of **1** along its *c*-axis at a frequency of 50 Hz, corresponding to applied electric fields of 34 (red), 40 (black), 43 (blue), and 49 kV cm^{-1} (magenta).

polarization was increased by increasing the electric field from 34 to 49 kV cm^{-1} (Fig. S12†), probably owing to the relatively large and gradually increased leakage currents under these electric fields, and the spontaneous polarization of 4.8 μC cm^{-2} at an electric field of 49 kV cm^{-1} was not saturated yet. Unfortunately, applying a higher electric field caused a short-cut current and the breakdown of the crystals, probably owing to the crystal defects and frangibility. In addition, the technical difficulty to apply an electric field exactly along the polar axis of the test crystal for such a uniaxial ferroelectric may also cause such kind of slanted P–E loops.

To gain an insight into the distinct polarization directions of ferroelectric domains in the δ phase, the vertical and lateral PFM (VPFM and LPFM) mappings on the same area of a single crystal of **1** were obtained simultaneously, by applying a voltage perpendicular to the (001) plane (Fig. 6f). In the VPFM mode, an obvious bipolar domain pattern emerged in the phase image (Fig. 6c), suggesting the existence of two different polarization directions with an angle of 180° in the regions. Subsequently, the VPFM and LPFM mappings on the nearby area were obtained, from which the VPFM phase image shows a bipolar domain pattern while the LPFM one shows an approximate single-domain state (Fig. S8†). The different domain distributions between the VPFM and LPFM modes match well with the two supposed anti-parallel polarization directions in such a uniaxial ferroelectric being orientated along its polar axis, i.e., the c-axis. Moreover, when a voltage of 135 V was applied, a rectangle-shape phase loop (Fig. 6d) and a butterfly-shape amplitude loop (Fig. 6e) representing a typical characteristic for the 180° polarization switching of

domains were observed, further supporting ferroelectricity for the δ phase.

To further find out the underlying mechanism for the spontaneous polarization along the c-axis, Hirshfeld surface analysis[50] was performed for the organic cation in the δ phase. As shown in Fig. 7b and c, the N–H···F and C–H···F interactions are associated with about 88% of the Hirshfeld surface area, making a major contribution to the host–guest interactions, while the H···H contacts are associated with the rest 12% area, contributing to the guest–guest interactions. As shown in the Hirshfeld surfaces mapped with a normalized contact distance (d_{norm}, Fig. 7a), in which the contacts shorter and longer than van der Waals separations are shown as red and blue spots, respectively, the red spots are found to be mostly associated with the hydrogen-bonding interactions (or weak non-classic hydrogen-bonding interactions), such as N1–H···F (N1···F distance: 2.88–3.05 Å), N2–H···F (2.91–2.95 Å), C2–H···F11 (3.25 Å), and C5–H···F32 (3.13 Å), representing the main strong host–guest interactions between organic cations and the inorganic framework.

In the fingerprint plot (Fig. 7b) representing the distances from the surface to the nearest nucleus inside and outside the surface with individual (d_i, d_e) pairs, as shown in Fig. 7b, the left bottom region with a minimal (d_i, d_e) ≈ (0.8–1.0 Å, 1.1–1.3 Å) indicated that the strongest contacts are mainly associated with N–H···F contacts, while the points marked in red (indicating a large number of contacts) are mainly associated with C–H···F contacts. In comparison, for the paraelectric γ phase, both the red and green regions, corresponding to both C–H···F and N–H···F contacts, respectively, are distributed more dispersedly
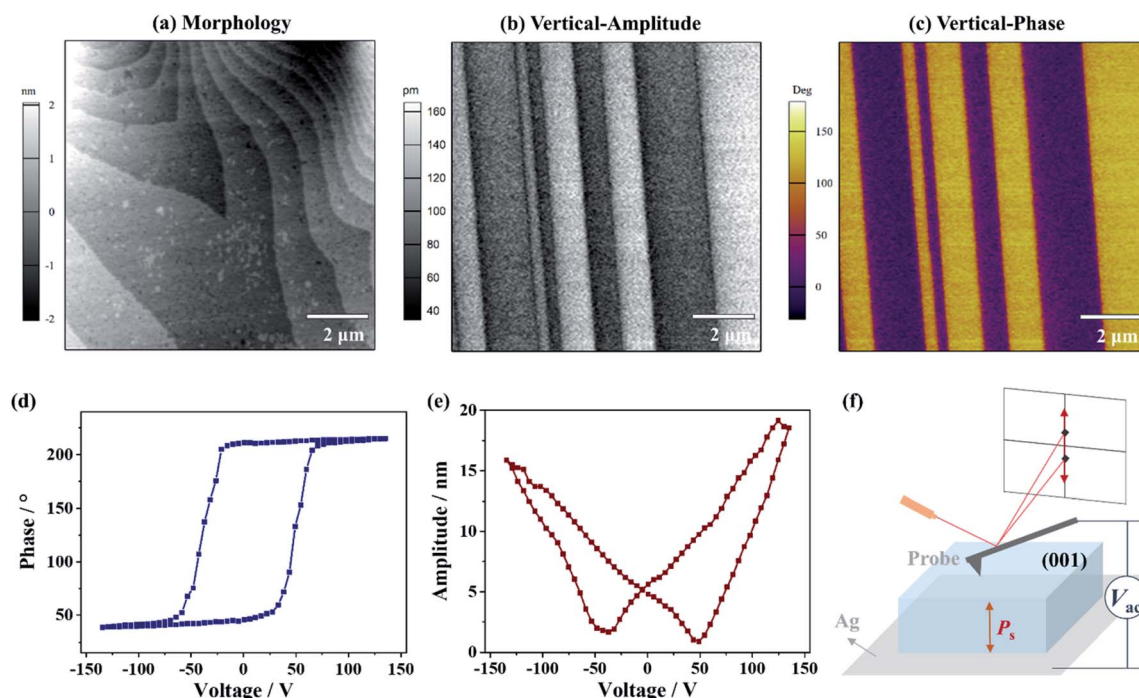

Fig. 6 Morphology image (a) and vertical (b and c) PFM images of the crystal surface for **1**. Phase-voltage hysteresis loop (d) and amplitude-voltage butterfly loop (e) for a selected point on the crystal surface. (f) Schematic diagram of the orientation for PFM measurements.
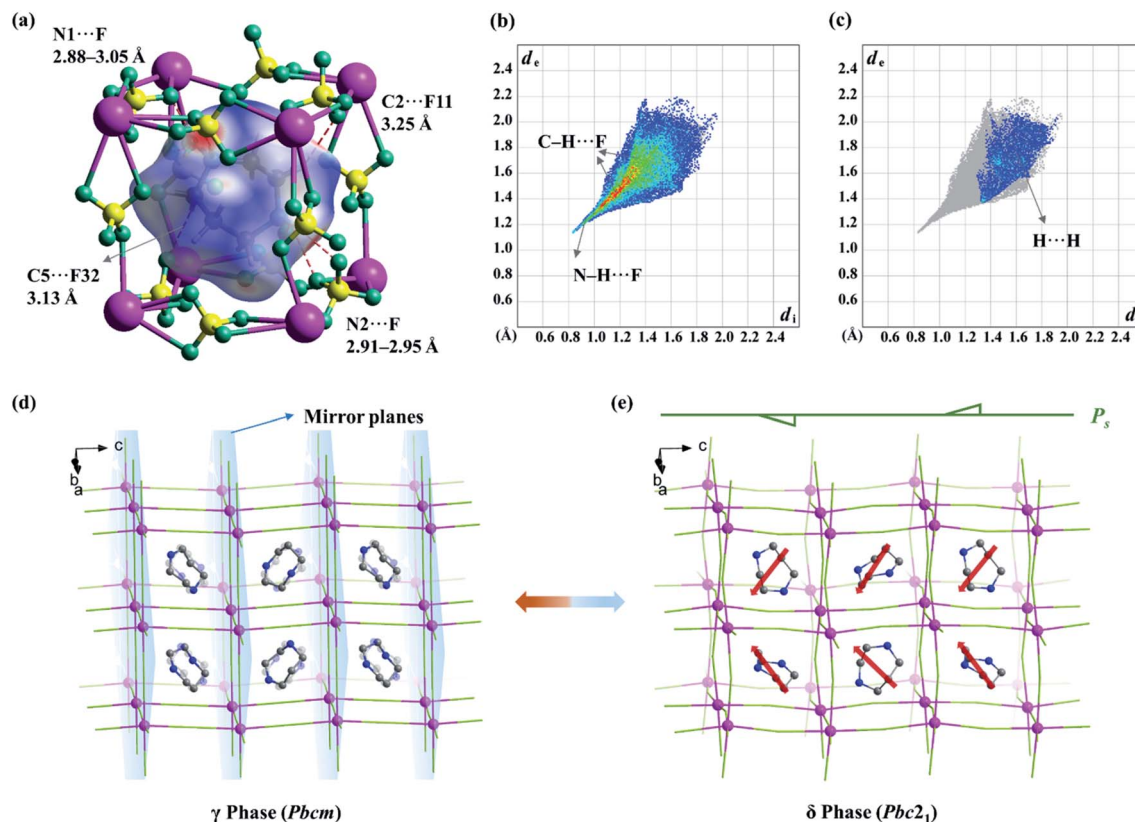
Fig. 7 (a) Hirshfeld surfaces mapped with d_{norm} over the range of -0.50 (red) to 0.90 (blue) for the guest cation at the δ phase. Fingerprint plot for H⋯F contacts (b) and H⋯H contacts (c) of guest cations at the δ phase. Crystal structures at 338 K (γ phase, d) and 293 K (δ phase, e) along the diagonal of the (001) lattice plane. For clarity, H atoms are omitted. In the γ phase, the organic cations are located in two sites about the mirror planes (light blue planes). In the δ phase, the orientations of ordered organic cations (the directions of dipole moment are shown in red arrows) induce spontaneous polarization along the c-axis and the disappearance of the mirrors in the δ phase.

(Fig. S6†), owing to the 2-fold positional disorder of organic cations.

The above information suggested that the host–guest interactions, *i.e.*, the strongest interactions produced by the two $-NH_2-$ groups of the H_2hpz^{2+} cation and numerous additional weak interactions produced by the five $-CH_2-$ groups, lead to the polar orientation of the guest cation in the δ phase. In detail, two $-NH_2-$ groups point exactly to the two BF_4^- bridges parallel to the diagonal of the unit cage and the ordered cation slantwise resides in the cage. As a result, the oriented ordered arrangement of the polar H_2hpz^{2+} cations together with an aforementioned deformation of the inorganic framework breaks the mirror symmetry and gives rise to spontaneous polarization along the c-axis in the δ phase (Fig. 7d and e). By contrast, the reported analogue, $(H_2mdabco)(NH_4)(BF_4)_3$,[35] containing a similar polar A-site cation with a dipole moment of *ca.* 1.6 D, undergoes a ferroelastic phase transition (with an Aizu notation of $m3mF\bar{3}m$) but not a ferroelectric one, as the adjacent branch-like rigid $H_2mdabco^{2+}$ cations adopt an opposite direction to cancel polarization. In another analogue, $(H_2pz)[Na(BF_4)_3]$,[34] the only one instance revealing a polar crystal structure ($P4_3$), its flexible A-site H_2pz^{2+} cations adopt a weak-dipolar configuration (*ca.* 0.02 D), and thus its polarity is mainly generated by the slight deformation of the framework. These facts suggest that,

distinguishing from the H_2pz^{2+} and $H_2mdabco^{2+}$ cations, the H_2hpz^{2+} cation combines a relatively larger dipole moment (*ca.* 2.1 D) and a more easily changeable configuration, and hence plays a crucial role in matching or inducing delicate framework deformation and eventually generating a reversible spontaneous polarization, *i.e.*, ferroelectricity, for **1**.

Conclusions

In summary, by using a polar cation with a relatively large dipole moment and an easy changeable conformation, *i.e.*, H_2hpz^{2+}, as an A-site cation to assemble with potassium tetrafluoroborate, we successfully obtained a new ABX_3-type tetrafluoroborate-based molecular perovskite, *i.e.*, **1**, which undergoes three-step phase transitions at 455 K, 384 K, and 311 K, respectively. By cooling the prototype cubic phase in which the A-site and X-site components are highly disordered, a stepwise change of molecular dynamics occurs, resulting in a ferroelastic phase featuring six equivalent ferroelastic domain states accompanied by an estimated spontaneous strain of 0.046. On further cooling the ferroelastic phase to room temperature, the organic cations are frozen thoroughly, resulting in ferroelectricity with a typical bipolar ferroelectric domain pattern. Such stepwise ferroelastic and ferroelectric phase

transitions in **1** benefit from the delicate interplay between the gradually frozen organic cations and the cooperatively deformed inorganic framework. As a unique instance with the coexistence of room-temperature ferroelastic and ferroelectric orders among the known molecular perovskites based on diverse bridges, **1** serves as an interesting example demonstrating a successful strategy to assemble high-temperature molecular multiferroics. Moreover, the present study provides important clues to guide the rational choosing of suitable organic cations and matchable B-site cations to assemble more advanced functional molecular perovskites based on tetrafluoroborate and other similar bridges.

Author contributions

W.-X. Zhang, X.-M. Chen and X.-X. Chen conceived the idea, designed the experiments and co-wrote the manuscript. X.-X. Chen performed the synthesis experiments, the Hirshfeld analysis, and the measurements of DSC, SHG, dielectric permittivity, crystal structures, ferroelastic domains and *P-E* hysteresis loops. X.-Y. Zhang and L.-Q. Xiong performed the PFM measurements. D.-X. Liu, R.-K. Huang and S.-S. Wang assisted the data collection and reduction of the variable-temperature crystal structures.

Conflicts of interest

There are no conflicts to declare.

Acknowledgements

Notes and references

1 W. Prellier, M. P. Singh and P. Murugavel, *J. Phys.: Condens. Matter*, 2005, **17**, R803–R832.

2 H. Bea, B. Dupe, S. Fusil, R. Mattana, E. Jacquet, B. Warot-Fonrose, F. Wilhelm, A. Rogalev, S. Petit, V. Cros, A. Anane, F. Petroff, K. Bouzehouane, G. Geneste, B. Dkhil, S. Lisenkov, I. Ponomareva, L. Bellaiche, M. Bibes and A. Barthelemy, *Phys. Rev. Lett.*, 2009, **102**, 217603.

3 Y. Tokunaga, N. Furukawa, H. Sakai, Y. Taguchi, T. H. Arima and Y. Tokura, *Nat. Mater.*, 2009, **8**, 558–562.

4 J. F. Scott, *Science*, 2007, **315**, 954–959.

5 S. Horiuchi and Y. Tokura, *Nat. Mater.*, 2008, **7**, 357–366.

6 G. F. Nataf, M. Guennou, J. M. Gregg, D. Meier, J. Hlinka, E. K. H. Salje and J. Kreisel, *Nat. Rev. Phys.*, 2020, **2**, 634–648.

7 M. Owczarek, K. A. Hujsak, D. P. Ferris, I. Majerz, P. Szklarz, H. Zhang, A. A. Sarjeant, C. L. Stern, R. Jakubas, S. Hong, V. P. Dravid and J. F. Stoddart, *Nat. Commun.*, 2016, **7**, 13108.

8 L. W. Martin and A. M. Rappe, *Nat. Rev. Mater.*, 2017, **2**, 16087.

9 G.-K. Long, R. Sabatini, M. I. Saidaminov, G. Lakhwani, A. Rasmita, X.-G. Liu, E. H. Sargent and W.-B. Gao, *Nat. Rev. Mater.*, 2020, **5**, 423–439.

10 O. Sato, *Nat. Chem.*, 2016, **8**, 644–656.

11 Q. Pan, Z.-B. Liu, Y.-Y. Tang, P.-F. Li, R.-W. Ma, R.-Y. Wei, Y. Zhang, Y.-M. You, H.-Y. Ye and R.-G. Xiong, *J. Am. Chem. Soc.*, 2017, **139**, 3954–3957.

12 H.-Y. Ye, Y.-Y. Tang, P.-F. Li, W.-Q. Liao, J.-X. Gao, X.-N. Hua, C. Hu, P.-P. Shi, Y.-M. You and R.-G. Xiong, *Science*, 2018, **361**, 151–155.

13 Y.-Y. Tang, P.-F. Li, W.-Q. Liao, P.-P. Shi, Y.-M. You and R.-G. Xiong, *J. Am. Chem. Soc.*, 2018, **140**, 8051–8059.

14 H.-Y. Zhang, Y.-Y. Tang, P.-P. Shi and R.-G. Xiong, *Acc. Chem. Res.*, 2019, **52**, 1928–1938.

15 W. Li, Z.-M. Wang, F. Deschler, S. Gao, R. H. Friend and A. K. Cheetham, *Nat. Rev. Mater.*, 2017, **2**, 16099.

16 W. Li, A. Stroppa, Z.-M. Wang and S. Gao, *Hybrid organic–inorganic perovskites*, WILEY-VCH Verlag GmbH & Co. KGaA, 2020.

17 W.-J. Xu, S. Kopyl, A. Kholkin and J. Rocha, *Coord. Chem. Rev.*, 2019, **387**, 398–414.

18 P. Jain, V. Ramachandran, R. J. Clark, H.-D. Zhou, B. H. Toby, N. S. Dalal, H. W. Kroto and A. K. Cheetham, *J. Am. Chem. Soc.*, 2009, **131**, 13625–13627.

19 M.-M. Zhao, L. Zhou, P.-P. Shi, X. Zheng, X.-G. Chen, J.-X. Gao, L. He, Q. Ye, C.-M. Liu and D.-W. Fu, *Chem.–Eur. J.*, 2019, **25**, 6447–6454.

20 L. C. Gomez-Aguirre, B. Pato-Doldan, A. Stroppa, L. M. Yang, T. Frauenheim, J. Mira, S. Yanez-Vilar, R. Artiaga, S. Castro-Garcia, M. Sanchez-Andujar and M. A. Senaris-Rodriguez, *Chem.–Eur. J.*, 2016, **22**, 7863–7870.

21 X.-H. Zhao, X.-C. Huang, S.-L. Zhang, D. Shao, H.-Y. Wei and X.-Y. Wang, *J. Am. Chem. Soc.*, 2013, **135**, 16006–16009.

22 Y.-Z. Hu, L. You, B. Xu, T. Li, S. A. Morris, Y.-X. Li, Y.-H. Zhang, X. Wang, P. S. Lee, H.-J. Fan and J.-L. Wang, *Nat. Mater.*, 2021, **20**, 612–617.

23 W.-J. Xu, Z.-Y. Du, W.-X. Zhang and X.-M. Chen, *CrystEngComm*, 2016, **18**, 7915–7928.

24 W.-J. Xu, P.-F. Li, Y.-Y. Tang, W.-X. Zhang, R.-G. Xiong and X.-M. Chen, *J. Am. Chem. Soc.*, 2017, **139**, 6369–6375.

25 Z.-Y. Du, T.-T. Xu, B. Huang, Y.-J. Su, W. Xue, C.-T. He, W.-X. Zhang and X.-M. Chen, *Angew. Chem., Int. Ed.*, 2015, **54**, 928–932.

26 K.-P. Xie, W.-J. Xu, C.-T. He, B. Huang, Z.-Y. Du, Y.-J. Su, W.-X. Zhang and X.-M. Chen, *CrystEngComm*, 2016, **18**, 4495–4498.

27 C. Shi, J.-J. Ma, J.-Y. Jiang, M.-M. Hua, Q. Xu, H. Yu, Y. Zhang and H.-Y. Ye, *J. Am. Chem. Soc.*, 2020, **142**, 9634–9641.

28 M. Mączka, A. Gągor, M. Ptak, D. Stefańska and A. Sieradzki, *Phys. Chem. Chem. Phys.*, 2018, **20**, 29951–29958.

29 S.-S. Wang, X.-X. Chen, B. Huang, R.-K. Huang, W.-X. Zhang and X.-M. Chen, *CCS Chem.*, 2019, **1**, 448–454.

30 S.-L. Chen, Z.-R. Yang, B.-J. Wang, Y. Shang, L.-Y. Sun, C.-T. He, H.-L. Zhou, W.-X. Zhang and X.-M. Chen, *Sci. China Mater.*, 2018, **61**, 1123–1128.

31 Y. Shang, R.-K. Huang, S.-L. Chen, C.-T. He, Z.-H. Yu, Z.-M. Ye, W.-X. Zhang and X.-M. Chen, *Cryst. Growth Des.*, 2020, **20**, 1891–1897.

32 W.-X. Zhang, S.-L. Chen, Y. Shang, Z.-H. Yu and X.-M. Chen, *Energy Mater. Front.*, 2020, **1**, 123–135.

33 G.-Z. Liu, J. Zhang and L.-Y. Wang, *Synth. React. Inorg., Met.-Org., Nano-Met. Chem.*, 2011, **41**, 1091–1094.

34 Y.-L. Sun, X.-B. Han and W. Zhang, *Chem.–Eur. J.*, 2017, **23**, 11126–11132.

35 G.-M. Fan, C. Shi, L. Qiao, H.-J. Li and H.-Y. Ye, *J. Mater. Chem. C*, 2018, **6**, 8349–8352.

36 L. Ye, Z.-X. Gong, C. Shi, J.-J. Ma, H. Liang, F.-W. Qi, D.-Y. E, C.-F. Wang, Y. Zhang and H.-Y. Ye, *CrystEngComm*, 2019, **21**, 7043–7047.

37 L.-L. Chu, T. Zhang, W.-Y. Zhang, P.-P. Shi, J.-X. Gao, Q. Ye and D.-W. Fu, *J. Phys. Chem. Lett.*, 2020, **11**, 1668–1674.

38 O. V. Dolomanov, L. J. Bourhis, R. J. Gildea, J. A. K. Howard and H. Puschmann, *J. Appl. Crystallogr.*, 2009, **42**, 339–341.

39 G. M. Sheldrick, *Acta Crystallogr., Sect. C: Struct. Chem.*, 2015, **71**, 3–8.

40 A. M. Glazer, *Acta Crystallogr., Sect. B: Struct. Crystallogr. Cryst. Chem.*, 1972, **28**, 3384–3392.

41 A. L. Goodwin, *Phys. Rev. B: Solid State*, 2006, **74**, 134302.

42 H. L. Bostrom, J. A. Hill and A. L. Goodwin, *Phys. Chem. Chem. Phys.*, 2016, **18**, 31881–31894.

43 S. G. Duyker, J. A. Hill, C. J. Howard and A. L. Goodwin, *J. Am. Chem. Soc.*, 2016, **138**, 11121–11123.

44 A. M. Glazer and K. Ishida, *Ferroelectrics*, 1974, **6**, 219–224.

45 K. Aizu, *J. Phys. Soc. Jpn.*, 1969, **27**, 387–396.

46 Z.-Y. Du, Y.-P. Zhao, C.-T. He, B.-Y. Wang, W. Xue, H.-L. Zhou, J. Bai, B. Huang, W.-X. Zhang and X.-M. Chen, *Cryst. Growth Des.*, 2014, **14**, 3903–3909.

47 S.-Y. Zhang, X. Shu, Y. Zeng, Q.-Y. Liu, Z.-Y. Du, C.-T. He, W.-X. Zhang and X.-M. Chen, *Nat. Commun.*, 2020, **11**, 2752.

48 J. Sapriel, *Phys. Rev. B: Solid State*, 1975, **12**, 5128–5140.

49 Y.-S. Zhao, D. J. Weidner, J. B. Parise and D. E. Cox, *Phys. Earth Planet. Inter.*, 1993, **76**, 17–34.

50 M. A. Spackman and D. Jayatilaka, *CrystEngComm*, 2009, **11**, 19–32.